Aberystwyth University

Sea surface wind retrieval in coastal areas by means of Sentinel-1 and numerical weather prediction model data

Rana, Fabio Michele; Adamo, Maria; Lucas, Richard; Blonda, Palma

Sea surface wind retrieval in coastal areas by means of Sentinel-1 and numerical weather prediction model data

Fabio Michele Rana[a,*], Maria Adamo[a], Richard Lucas[b], Palma Blonda[a]

[a] CNR-Institute of Atmospheric pollution (IIA), Bari, Italy
[b] Institute of Geography and Earth Sciences, Aberystwyth University, Aberystwyth, Ceredigion SY23 2EJ, United Kingdom

ABSTRACT

The present paper applies Synthetic Aperture Radar (SAR) based on Local Gradient-Modified (LG-Mod) algorithm to retrieve wind directions from Sentinel-1 data in the Camargue and the Wadden Sea protected coastal areas. Wind speeds are estimated through the inversion of the C-band MODel 5.N (CMOD5.N) backscattering model. Both Interferometric Wide Swath (IW) and Extra Wide Swath (EW) Level 1 products were evaluated for wind fields retrieval at high (5 km) and medium (12.5 km) output spatial resolutions. SSW fields from Sentinel-1 were compared with Numerical Weather Prediction (NWP) models and in situ data. Exploitation of the LG-Mod provided wind direction with a related marginal error parameter (i.e., ME_α^{ROI}) which proved useful for selecting the optimal input pixel size of SAR data processing. When compared to in situ data, the selection of the optimal pixel size reduced the Root Mean Squared Error (RMSE) values of LG-Mod wind directions up to 7° and about 45° for Wadden Sea and the Camargue site, respectively. In turn, such reduction provided a decrease of the wind speed RMSE values up to 0.7 m/s and 2.1 m/s, for Wadden Sea and the Camargue site, respectively. In addition, the LG-Mod gave better performance than the global NWP model European Centre for Medium-Range Weather Forecasts (ECMWF) in estimation of wind direction, at 12.5 km output spatial resolution, for both sites. The ME_α^{ROI} exploitation in the directional analysis of IW and EW products evidenced that at high resolution (5 km) the percentage of reliable wind directions from IW images (84.5%) resulted much larger than that obtained from EW images (30.1%). At medium resolution (12.5 km) instead, the percentage values resulted quite close to each other (99.2% and 86.3%, respectively). IW images proved optimal for high resolution SSW retrieval, whereas EW images suitable for medium resolution. With respect to NWP models, the spectral analysis confirmed the suitability of Sentinel-1 to represent the local wind fields spatial variability in coastal areas, at both high and medium output resolution. Our findings suggest that the combination of the LG-Mod algorithm with NWP models could better resolve spatially wind patterns in complex coastal areas.

1. Introduction

Sea Surface Wind (SSW) speed and direction can be considered essential variables in the monitoring of coastal ecosystems as well as in the planning of conservation and restoration actions in protected areas (Borrelli et al., 2017). Ecological models can support such actions, but the assimilation of SSW measurements would require their coupling with wind accuracy estimates.

Beside localized in situ measurements, most techniques for SSW retrieval have relied on both Numerical Weather Prediction (NWP) models and Synthetic Aperture Radar (SAR) (Dagestad et al., 2012; Monaldo et al., 2013). Several methodologies have been used for the exploitation of SAR imagery in the retrieval of both the direction (Wackerman et al., 2003; Koch, 2004; Zecchetto and De Biasio, 2008;

Rana et al., 2016) and speed of SSW (Mouche et al., 2012; Zhang et al., 2012; Benassai et al., 2015; Komarov et al., 2014). Among the techniques suggested, the one most used relies on the so-called scatterometry-based approach, which involves two steps: first, the wind direction is either retrieved from NWP, provided by in situ stations or extracted from SAR images models (Pichel et al., 2015; Monaldo et al., 2015). Then, assuming wind direction as a-priori information, wind speed can be inferred through the inversion of backscattering semi-empirical models, i.e., Geophysical Model Functions (GMFs) (Stoffelen and Anderson, 1997; Hersbach, 2010; Li and Lehner, 2014).

Recently, both the United States National Oceanic and Atmospheric Administration (NOAA) and the Copernicus programme have used the scatterometry-based approach to analyze new Sentinel-1 SAR data (Mouche, 2011; Monaldo et al., 2015). Although operational, the

---

techniques used by NOAA and Copernicus relay on NWP models for wind direction retrieval, they can meet problems when used in coastal areas. On the one hand, the local orography can affect the accuracy of the wind direction retrieved through NWP models, but on the other, the impact that bathymetry, surface currents, temperature gradients and wave features can have on sea surface roughness may hamper SAR backscattering (Zecchetto et al., 2016). Accounting for the effects of all these factors remains problematic and in need of further investigation (Ahsbahs et al., 2017).

Techniques for SSW direction retrieval from SAR data can be applied only when specific wind patterns, termed wind rows in the present study, are visible on SAR amplitude images (Alpers and Brümmer, 1994). The patterns in question include:

1. The rows produced by boundary layer rolls (BLRs) which are determined by thermal and dynamic air-sea instability and occur with typical wind speed values of about 15 m/s (Levy, 2001; Drobinski and Foster, 2003; Svensson et al., 2017). The BLRs axes are general between the direction of the mean sea surface wind and that of the associated geostrophic wind (Alpers and Brümmer, 1994).

2. The rows due to the presence of either elongated convective cells, wind-driven Langmuir cells, orography inhomogeneity, or wind-distributed surfactants. These rows, commonly named wind streaks (WSs), are closely aligned with the mean sea surface wind directions (Dankert et al., 2003; Koch and Feser, 2006; Svensson et al., 2017).

The physical mechanism producing wind rows can induce SAR backscattering modulations with spatial scales ranging from 0.1 to about 8 km (Dankert et al., 2003; Koch, 2004). As a consequence, appropriate pixel-size (scale) of SAR data processing must be identified for reliable wind direction retrieval.

Several studies report that the probability of BLRs visibility on SAR images can range from 35% (Levy, 2001) to 48% (Zhao et al., 2016), depending on the season of observation (Zhao et al., 2016). To our knowledge, very little reliable information is available on the occurrence of WSs.

In spite of limited wind patterns visibility occurrence, several SAR wind direction retrieval algorithms have been proposed in the literature (Wackerman et al., 2003; Du et al., 2002; Fichaux and Ranchin, 2002; Zecchetto and De Biasio, 2008; Leite et al., 2010). One of the most useful algorithms available derives the orientation of wind-aligned structures by computing local gradients (LGs) from SAR amplitudes at different scales (Koch, 2004). This approach has been validated against both in situ observations and NWP model data, with an output directional accuracy equal to 20–30° on ENVISAT ASAR data (Horstmann and Koch, 2004). La et al. (2017) have proved that the LG method can yield 1–5 km spatial resolution wind fields. Therefore, it seems reasonable to select a LG-family method for coastal areas where high resolution wind estimation is required.

The present study applies a modified Local Gradient (LG-Mod) algorithm (Rana et al., 2016) for wind direction retrieval from SAR Sentinel-1 (S-1) imagery in two protected coastal areas, which are characterized by different orography and wind regimes, namely, the Camargue (France) and the Wadden Sea (Netherlands). The study also investigates the use of wind direction retrieved from S-1 for wind speed estimation through GMF.

The LG-Mod algorithm models the observed local gradient directions with a diametrically bimodal distribution. Thus, by adapting results from Directional Statistics to axial data (Fisher, 1993), it allows the estimation of the dominant wind direction within each examined sub-image (or ROI). Moreover, the LG-Mod can determine each wind directional estimate along with its associated error, i.e., the marginal error ME_α^{ROI}.

In a previous study, Rana et al. (2016) investigated the usefulness of the ME_α^{ROI} parameter in automatic selection of SAR (i.e., ASAR) images which present wind rows patterns. In the present study, the same parameter will be exploited to provide: a) an error map of the retrieved wind directions output; b) an optimal SAR processing pixel-size for wind rows scale matching; c) a threshold value, i.e. ME^{TH}, to identify reliable wind direction estimates; d) a directional performance analysis of the Interferometric Wide Swath Ground Range Multi-Look Detected High Resolution (henceforth IW) and the Extra-Wide Swath Ground Range Multi-Look Detected Medium Resolution (henceforth EW) Sentinel-1 products in view of the output wind spatial resolution (i.e., high 5 km and medium 12.5 km grids).

Afterward, SSW fields derived from both S-1 and NWP models will be compared first with in situ data by determining the Root Mean Squared Error (RMSE) and Mean Bias Error (MBE). Then, to evaluate their capability to better resolve spatial variability of coastal local wind patterns, SSW from S-1 and NWP models will be compared to each other by using both statistics and spectral analysis.

The paper is organized as follows: Section 2 describes the study areas; Section 3 introduces the S-1 dataset considered, the NWP models used for results comparison and the available in situ wind measurements; Section 4 presents the methodology adopted for extracting wind direction and speed from SAR data, and for wind fields comparison criteria; Sections 5 presents results and Section 6 provides their discussion; Section 7 reports the conclusions.

2. Study areas

The Wadden Sea and the Camargue coastal areas whose winds are investigated in this study belong to the European Natura 2000 network (http://ec.europa.eu/environment/nature/natura2000).

The Wadden Sea site includes the Dutch Wadden Sea Conservation Area, the German Wadden Sea National Parks of Lower Saxony and Schleswig-Holstein, and most of the Danish Wadden Sea maritime conservation area (Fig. 1a). The site extends over 4700 km2 characterized by extensive tidal mud flats, saltmarshes, and deeper tidal creeks between the mainland and a chain of islands, which denote the outer boundary between the Wadden and North Sea (http://www.ecopotential-project.eu/2016-05-24-14-52-12/protected-areas.html).
In this area beaches and dunes are significant geomorphologic elements that can protect coastal areas from erosion processes. Dunes are formed by Aeolian sand transport from dry beach areas. At higher wind velocities, sand grains are transported in the wind direction, with the wind-born particles settling and accumulating where the wind speed decreases (CPSL, 2005).

The Camargue Biosphere Reserve, located in the Gulf of Lions (Fig. 1b), is surrounded by relatively high mountains (i.e., the Pyrenees, the Massif Central and the Alpes) interrupted by valleys. The site covers 1930km^2 and includes 50% of natural and semi-natural habitats dominated by lagoons, brackish/freshwater open and reed marshes, halophilous steppes, rangelands and fallow lands. The Camargue coastline is subjected to significant erosion (https://tourduvalat.org/en/actions/gestion-adaptative-etangs-marais-salins-de-camargue/).
The mountains surrounding the area influence the winds of this region, mostly the Mistral (blowing from North-West) and the Tramontane (from North) (Fig. 2). These winds are strong and highly transient in speed, with a stable offshore direction and a short lifetime (Millot, 1979).

In view of the important role that winds have in the dynamic of both the Wadden Sea and Camargue sites, long term monitoring of wind fields could benefit the design of adequate coastal conservation/regeneration actions (https://www.climatechangepost.com/netherlands/coastal-erosion/), as well as the evaluation of climate changes impact on the areas.

3. Datasets

The SAR dataset considered for both study sites, consists of several C-band images, acquired by the two-satellite constellation Sentinel-1
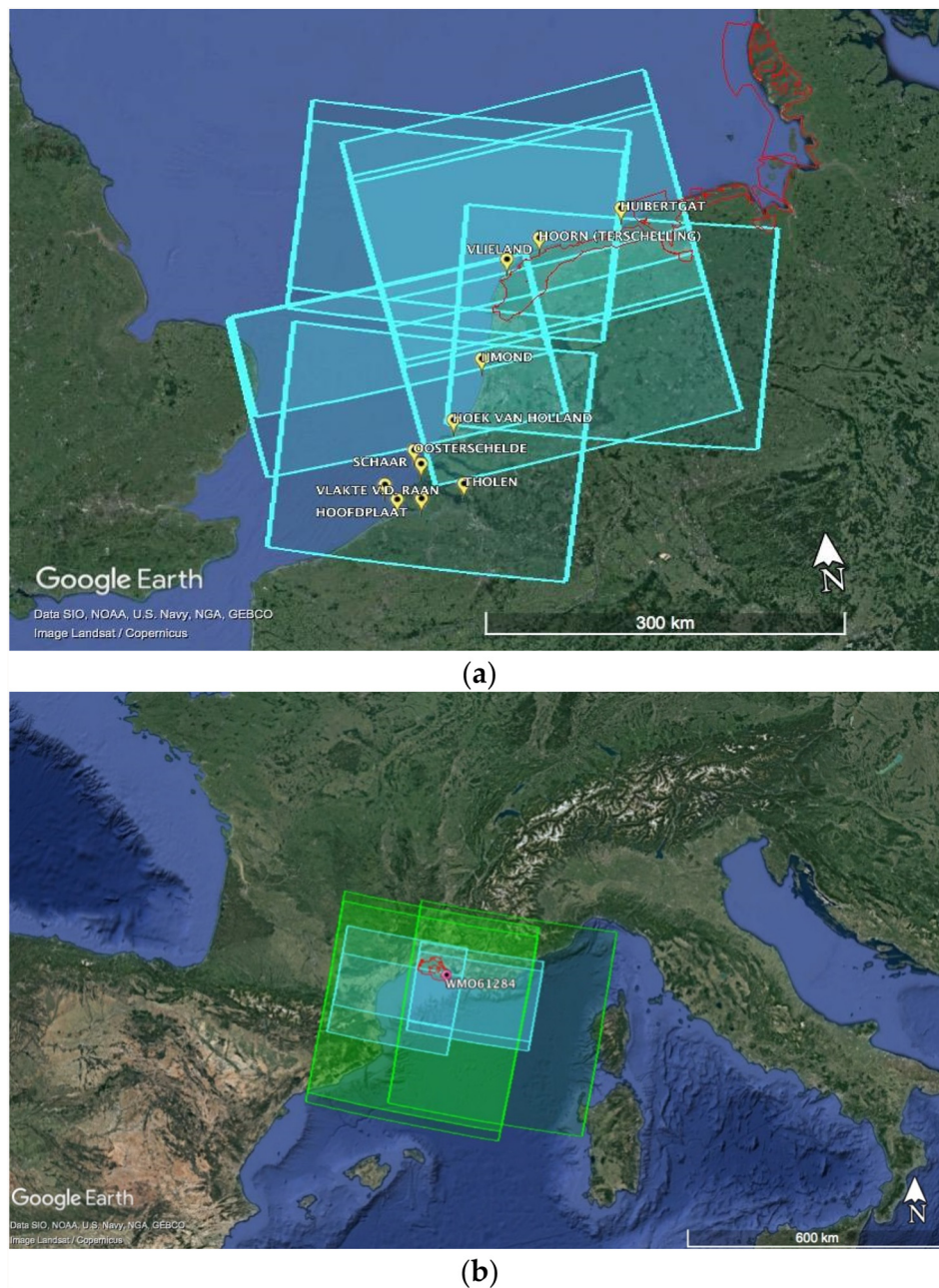
Fig. 1. Study areas: (a) Wadden Sea (red line contour), Dutch Delta and south-western area along North Sea shores, with 11 coastal KNMI wind measurement stations (yellow black-dotted icons). (b) Camargue (red line contour) in the Gulf of Lions, with 1 coastal IFREMER wind measurement buoy (yellow black-dotted icon). Sentinel-1 full-frames shown in green and cyan for EW and IW images, respectively. Background images (Data SIO, NOAA, U.S. Navy, NGA, GEBCO; Image Landsat/Copernicus) are from Google Earth. (For interpretation of the references to colour in this figure legend, the reader is referred to the web version of this article.)

(i.e., S1-A and S1-B). Different image mode and resolution class Level 1 products, i.e. IW and EW images, were downloaded from the Copernicus Open Access Hub (https://scihub.copernicus.eu). These images are characterized by well-visible wind rows near the coast. The selected scenes (Table 1) include images from December 2014 to March 2017 for The Wadden Sea site and from December 2014 to May 2016 for the Camargue site. The selection corresponds to 5% and 10% of all the data available for the former and the latter site, respectively. For both sites, the percentage of occurrences of wind rows in the images analyzed results lower than the ones reported in Levy (2001) and Zhao et al. (2016), i.e., 35% and 48% respectively. This may be due to the fact that our study concerns only coastal wind rows in two small areas where local wind conditions could have influenced wind rows visibility.

For both study areas, co-located 10-meter wind direction and speed were extracted from the global European Centre for Medium-Range Weather Forecasts (ECMWF) Interim *Re*-Analysis (ERA-Interim) archive (Dee et al., 2011; http://www.ecmwf.int). The archive makes available daily global re-analyses of wind data, every 6 h (i.e., 00 h:00, 06 h:00, 12 h:00, 18 h:00 UTC) and with a regular resampled grid of about $0.125° \times 0.125°$ (latitude × longitude). For the Camargue area, wind measurements from the regional Cyprus Coastal Ocean Forecasting and Observing System (CYCOFOS) weather system (Zodiatis et al., 2003; http://www.oceanography.ucy.ac.cy/cycofos/index.html) were available as well. Based on the SKIRON model (Kallos et al., 1997), the CYCOFOS database furnishes the daily predictions over the Western Mediterranean Sea, every hour with a spatial grid of about $0.05° \times 0.05°$. The wind speed data available were provided by both NWP models as non-neutral (i.e., stability dependent) values.
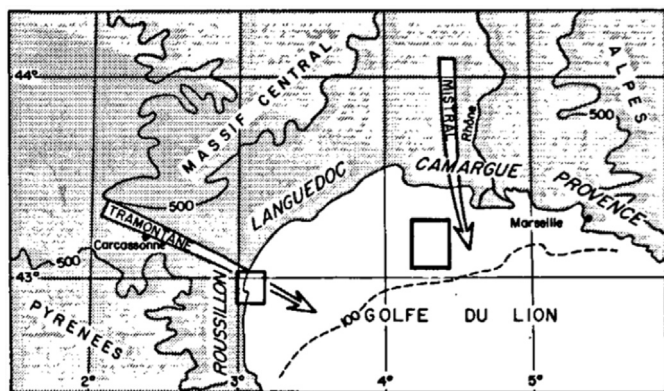
Fig. 2. Gulf of Lions: the Mistral (from NW) and the Tramontane (from N) winds (Millot, 1979).

For the Wadden Sea site, in situ wind observations were provided as 10-min averages (i.e., 00 h:00, 00 h:10, etc.) by the stations of Koninklijk Nederlands Meteorologisch Instituut (KNMI) (http://www.knmi.nl/home). Each station was equipped with an anemometer for wind speed (range: 0.5–50 m/s; resolution: 0.1 m/s; accuracy: ± 0.5 m/s) and direction (range: 0°-360°; resolution: 1°; accuracy: ± 3°) measurements (Nederlands, 2000).

KNMI measurements were exploited as "ground truth" for validation purposes. These wind observations were gathered by 11 coastal marine and land-based stations (Fig. 1a), matching in time and space with the Sentinel-1 acquisitions (Table 1). Relevant information about KNMI stations deployment and anemometers positioning are presented in Table 2.

For the Camargue site, a number of in situ wind observation archives were investigated; these include: a) the NOAA National Data Buoy Centre (NOAA NDBC) (http://www.ndbc.noaa.gov/); b) the Meteo France Catalogue (https://donneespubliques.meteofrance.fr/); c) the Institut Français de Recherche pour l'Exploitation de la Mer (IFREMER) Buoys Data Base.

The NOAA NDBC reports no coastal wind observations. The only data available concern buoys located offshore, namely, Nice and Lion. The Meteo France Catalogue reports mainly wind measurements recorded by seafaring ships. These measurements cannot be considered adequate for comparison with Sentinel-1 SSW estimates due to the

variations of ship position over time as well as to the poor resolution of the wind recorded (i.e., 1 m/s for wind speed and 10° for wind direction). The IFREMER Buoys Data Base, which is part of the Copernicus Marine Environment Monitoring Service (http://www.mongoos.eu/data-center), provides only 9 observations co-located, in time and space, with the selected Sentinel-1 images (Table 1). These data are acquired every 6 h by a single moored buoy (Fig. 1b) equipped with an anemometer for wind speed (resolution: 0.001 m/s) and direction (range: 0°-360°; resolution: 1°) measurements. Table 2 presents details about the IFREMER buoy measurements.

All in situ wind speed measurements were taken at 10 m above the (mean) sea level (a.s.l) and registered as non-neutral values.

4. Methodology

SAR data pre-processing and generation of auxiliary products (e.g. land-sea mask and incidence angle map) were performed using the Sentinel Application Platform (SNAP) from ESA (http://step.esa.int/main/toolboxes/snap/).

SAR data processing for wind direction and speed retrieval (Fig. 3) and the subsequent assessment of the output wind fields are described in Sections 4.1 to 4.4.

4.1. Wind direction retrieval from SAR data: LG-Mod

SSW direction retrieval from S-1 data was carried out through the LG-Mod algorithm. Since the details of this algorithm are described in (Rana et al., 2016), the present paper illustrates only specific aspects of the algorithm. These include:

A. *Bright and dark pixels masking.* The masking of either bright pixels or dark-spots is carried out by thresholding the LG amplitude. The thresholding is aimed at excluding those points characterized by strong local gradients that cannot be associated to either wind rows or SAR structures approximately aligned to the forcing wind.

B. *Main Wind Directions Estimates.* The main wind direction within a ROI, i.e. $\langle \beta^{ROI} \rangle$, and the associated marginal error, i.e. ME_α^{ROI} (with the confidence level (1-α) fixed by the user), are directly estimated from the set of the observed and usable LG directions computed inside the ROI itself. ME_α^{ROI} is a function of the Mean Resultant Length (R^{ROI}) (Rana et al., 2016). This is an a-dimensional scalar quantity and ranges from zero to one. R^{ROI} can be considered a

Table 1
Sentinel-1 SAR dataset.

Sentinel-1 date and time	Satellite pass	Sensor	Acquisition mode	Pixel spacing [Rng x Azi] [m x m]	Polarization
Wadden Sea					
20141212T055753	Descending	S1-A	IW	10 × 10	VV
20141227T173304	Ascending				HH
20150503T172442					VV
20151205T172503					
20151210T173303					
20160131T054930	Descending				
20161014T055741					
20161223T172515	Ascending				
20170112T055653	Descending	S1-B			
20170323T172426	Ascending				
Camargue					
20141207T055154	Descending	S1-A	EW	40 × 40	VV
20141226T054342					HH
20141231T055153					VV
20150124T055156					HH
20150205T055203			IW	10 × 10	VV
20160219T054400					
20160407T054404					
20160424T055219					
20160501T054405					

Table 2
Information about KNMI and IFREMER stations deployment and anemometers positioning.

| Site	Station ID	Source	Geographic coordinates (Lat/Lon) [°]	Reference height of anemometer [m] (a.s.l.)	Type of station	Distance from coastline [m]
Wadden Sea	209	KNMI	52.465 N/4.518 W	10.0	marine buoy	≈2000
	242		53.241 N/4.921 W	10.0	land-based mast	≈ − 810
	251		53.392 N/5.346 W	10.0	land-based mast	≈ − 3000
	285		53.575 N/6.399 W	10.0	marine buoy	≈2700
	308		51.381 N/3.379 W	10.0	marine buoy	≈205
	311		51.379 N/3.672 W	10.0	marine must	≈500
	312		51.768 N/3.622 W	10.0	marine buoy	≈6900
	313		51.505 N/3.242 W	10.0	marine buoy	≈13,500
	316		51.657 N/3.694 W	10.0	marine buoy	≈1500
	330		51.992 N/4.122 W	10.0	land-based mast	≈ − 700
	331		51.480 N/4.193 W	10.0	marine buoy	≈1800
Camargue	61,284	IFREMER	43.319 N/4.866E	10.0	moored buoy	≈2000
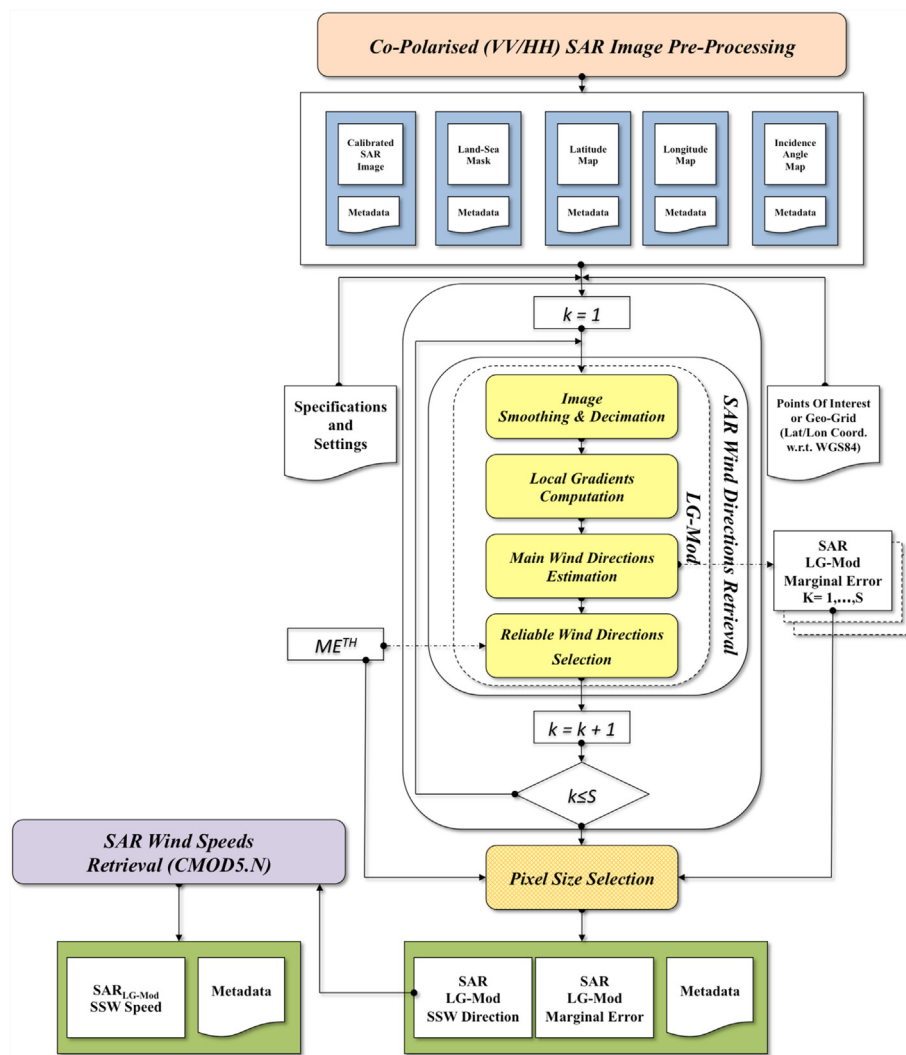
Fig. 3. SAR data pre-processing and SAR SSW fields retrieval.

measure of the local directions alignment (directional content) within the ROI (Fisher, 1993). In other words, the smaller the marginal error, the higher the directional content within the ROI and, hence, the better the accuracy of the directional estimates.

C. *Reliable Wind Directions Selection.* To obtain "reliable" output directions a suitable threshold of acceptance is set, i.e., a maximum marginal error value ME^{TH}. This threshold is applied to all LG-Mod directional outcomes: $\{ROI^{TH}\} = \{ME_\alpha^{ROI} \le ME^{TH}\}$. Whenever the threshold decreases, the number of reliable wind directions

decreases accordingly.

4.2. Directional analysis

The directional analysis first investigated the effectiveness of the ME_α^{ROI} in the selection of the optimal pixel size to be used for the processing of SAR data through LG-Mod (Section 5.1.1). The optimal input processing pixel size defined as the one which can yield the largest percentage value of reliable ROIs, i.e. the ROIs characterized by an
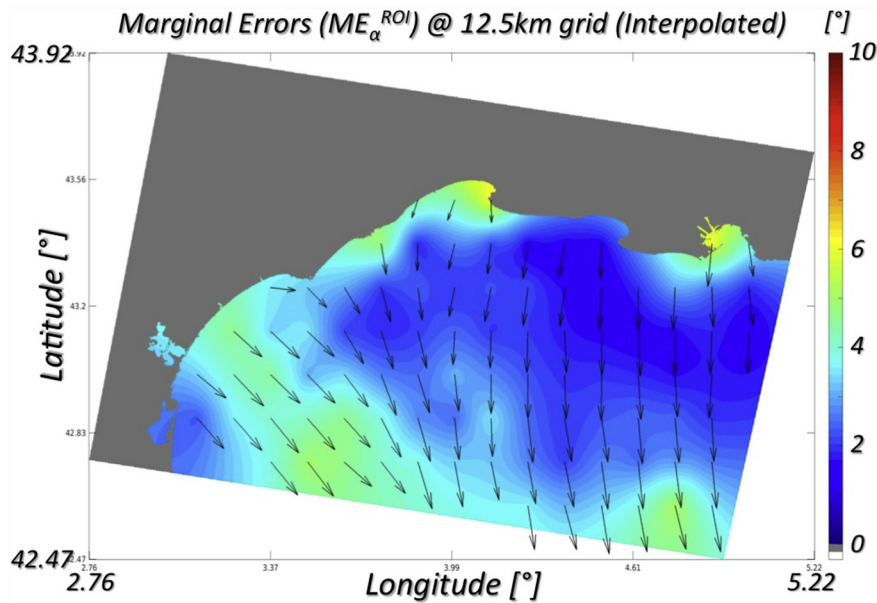
Fig. 4. Marginal error map at 12.5 km from a Sentinel-1 IW image, 5th Feb 2015. LG-Mod wind directions: black arrows. Camargue study area.

ME_α^{ROI} value less or equal to an established threshold ME^{TH}. This criterion was chosen in order to maximize not only the directional content of the whole image dataset considered, but also the accuracy of the wind direction outputs. Afterward, the analysis focused on the exploitation of EW and IW images at different output spatial resolutions, i.e., 5 km and 12,5 km (Section 5.1.2).

4.3. Wind speed retrieval from SAR data

Once the wind directions from either the LG-Mod, the NWP models, or the in situ measurements had been retrieved, the corresponding wind speeds were obtained by inverting the CMOD5.N. The resulting speed values were gauged at neutral atmospheric conditions (Hersbach, 2010). Atmospheric stability was not accounted for due to lack of additional data concerning air temperature, relative humidity, and sea surface temperature necessary to convert equivalent neutral stability wind speeds to stability dependent ones (Liu et al., 1979; Liu and Tang, 1996). In the literature, RMSE between neutral and non-neutral wind speed values has been reported to be quite low, i.e., from 0.2 to 0.3 m/s (La et al., 2017; Portabella and Stoffelen, 2009). Therefore, atmospheric stability correction may have negligible influence on our estimates.

For C-band HH-polarized SAR images, the GMF was used together with the Polarization Ratio (PR), defined as $PR = \frac{\sigma_{VV}^0}{\sigma_{HH}^0}$, where σ_{HH}^0 and σ_{VV}^0 are the HH– and VV-polarized Normalized Radar Cross Section (NRCS) respectively (Liu et al., 2013). The simple empirical formula proposed by Thompson et al. (1998), i.e. $PR = \frac{(1 + 2 \cdot \tan^2 \vartheta)^2}{(1 + \alpha \cdot \tan^2 \vartheta)^2}$, was adopted for HH-polarized images. To overcome the modelled NRCS over-estimation, the surface scattering parameter $\alpha = 1.2$ was used (Vachon and Dobson, 2000).

4.4. Wind fields assessment

Wind fields assessment was carried out by examining the output SSW fields with in situ data and NWP model outputs. First, SSW fields from both the Sentinel-1 and the ECMWF data were compared with in situ measurements for validation purposes (Section 5.2). SAR SSW direction and speed estimates were derived from ROIs centered on the nodes of the ECMWF 12.5 km grid. SAR and co-located ECMWF wind estimates were coupled with the available in situ measurements. As a result, 24 and 9 match-ups were obtained, for the Wadden Sea and the Camargue areas, respectively. For the mentioned coupling, the

following temporal and spatial proximity criteria were applied: 1) the maximum time delay between SAR estimates and in situ observations was set at about 5 min for KNMI data in the Wadden Sea, and 16 min for IFREMER data in the Camargue. For the former site, ECMWF and KNMI data were provided exactly at the same time. For the latter, IFREMER data were interpolated at ECMWF times; 2) the nearest distance between either SAR or ECMWF estimate and in situ observations was set at less than 9 km. The latter value was selected as the circumradius of each squared ROI, whose sides have length of 12.5 km.

Afterwards, a comparison between S-1 SSW field estimates and those from ECMWF was carried out at 12.5 km resolution, for both sites. The comparison at 5 km resolution with the SKIRON model was also done only for the Camargue site (Section 5.3). To avoid the spatial resampling of the wind values obtained by both NWP models, the SAR ROIs examined were centered at the points of their specific data grid. The wind data from NWP models were not temporally interpolated since each SAR acquisition time was quite close to the reference time of both ECMWF and SKIRON. Namely, min, mean and max delays $\Delta T_{SAR\text{-}ECMWF} \sim -2, -21$ and -35 min, for the former and $\Delta T_{SAR\text{-}SKIRON} \sim -8, -12$ and -16 min for the latter, respectively.

Root Mean Square Error (RMSE) and Mean Bias Error (MBE) were selected as summary statistics to evaluate the average performances of the different methods in the estimation of wind direction and speed. The Sample Number N, representing the number of samples used for the RMSE and MBE computation, is presented in Table 5. N was always obtained after the application of the directional threshold ME^{TH} to all the N^{TOT} SAR LG-Mod outcomes. In other words, N is the number of ROIs and the corresponding SAR LG-Mod wind directions assumed as reliable since they had a ME_α^{ROI} less or equal to the fixed ME^{TH}. Hence, N is the number of wind directions and speeds that were compared and $P = (N/N^{TOT})*100$ is the ROI selection percentage (Table 5).

5. Results

5.1. LG-Mod directional analysis

The outputs of the LG-Mod algorithm include the wind direction and the associated marginal error ME_α^{ROI} maps. Fig. 4 shows the output marginal error (ME_α^{ROI}) map obtained from a Sentinel-1 IW image (February 5th, 2015) by LG-Mod. The black arrows indicate the output LG-Mod wind directions.
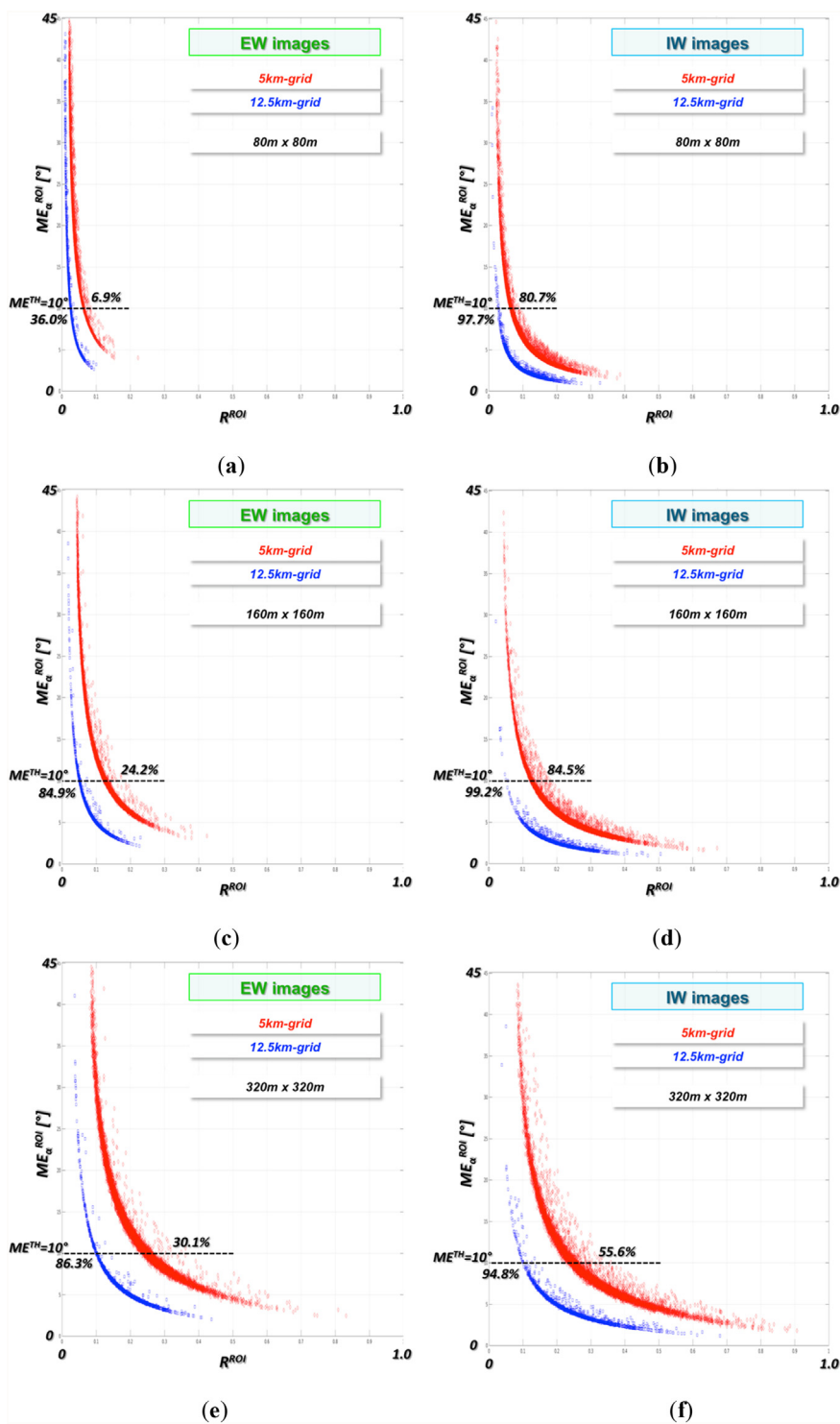
Fig. 5. Marginal error ME_α^{ROI} (y-axes), in degrees, versus the concentration parameter R^{ROI} (x-axes) at 5 km (red diamonds) and 12.5 km (blue squares). For Camargue EW images, (a), (c) and (e) refer to 80 m, 160 m and 320 m input pixel size, respectively. For IW images from both Camargue and Wadden Sea sites, figures (b), (d) and (f) refer to 80 m, 160 m and 320 m input pixel size, respectively. (For interpretation of the references to colour in this figure legend, the reader is referred to the web version of this article.)

Rana et al. (2016) have proved that the selection of reliable wind directions by thresholding ME_α^{ROI} can provide RMSE reduction for the comparison of LG-Mod and in situ directions.

For the Camargue site, both EW and IW images were analyzed, whereas for the Wadden Sea only IW data were used due to the lack of visible wind row patterns on the EW products.

Fig. 5 plots the marginal error measurements ME_α^{ROI} evaluated with

a requested 95% confidence level for each directional estimate. ME_α^{ROI} values are presented as a function of the concentration parameter R^{ROI}. Specifically, Fig. 5a, c and e refer to the EW dataset available for the Camargue site only. Fig. 5b, d and f correspond to the IW dataset available for both sites investigated. All the ROI considered were processed at three input pixel sizes, i.e. 80 m, 160 m and 320 m. In all the aforementioned figures, red diamonds and blue squares relate to LG-

Mod measurements obtained at 5 km and 12.5 km output resolutions, respectively.

5.1.1. Pixel size selection

The optimal input processing scale used, for each S-1 product, was selected according to the criterion described in Section 4.2. Fig. 5 evidences that:

- The optimal IW input pixel size resulted to be 160 m at both 5 km and 12.5 km output resolutions. In particular, at the highest output resolution (5 km), the ROI selection percentage values were 84.5%, 80.7% and 55.6% at 160 m (Fig. 5b), 80 m (Fig. 5d) and 320 m (Fig. 5f), respectively. At medium resolution grid (12.5 km), the percentage values were 99.2%, 97.7% and 94.8% at 160 m (Fig. 5b), 80 m (Fig. 5d) and 320 m (Fig. 5f), respectively.
- The optimal EW input pixel size was 320 m at both output spatial resolutions. At the highest resolution (5 km), the ROI selection percentage values were 30.1%, 6.9% and 24.2% at 320 (Fig. 5a), 80 m (Fig. 5c) and 160 m (Fig. 5e), respectively. At medium resolution (12.5 km grid), the percentages were 86.3%, 36% and 84.9% at 320 m (Fig. 4a), 80 m (Fig. 4c) and 160 m (Fig. 4e), respectively.

It is worth noting that the selection of the optimal pixel size allows the maximization of the number of reliable output directions within the whole image dataset analyzed. However, local changes in optimal pixel size selection can occur due to the fact that different mechanisms, such as BLRs and elongated convective cells, can induce wind aligned streaks on SAR images. As a consequence, wind rows may be characterized by NRCS modulations with wavelengths ranging from few hundred meters to few kilometres (Koch, 2004).

5.1.2. IW and EW images comparison

In general, at each input processing scale and output spatial resolution, the results reported clearly indicate that the marginal error values ME_α^{ROI} obtained from EW images (Fig. 5a, c and e) are always higher than those obtained from IW ones (Fig. 5a, c and e and Fig. 5b, d and f, respectively). As a consequence, once ME^{TH} had been fixed, the percentage of reliable wind directions from IW images were higher than the those from EW images. The difference between the IW and EW percentage values is higher at 5 km than at 12.5 km resolution (Fig. 5). This finding may be due to the different native spatial resolution of the two Sentinel-1 products.

5.2. SAR SSW fields and NWP model data versus in situ measurements

KNMI and IFREMER buoys used for validation cover a limited area of the S-1 images considered (Fig. 1). Hence, while in Section 5.1 all ROIs of each image were considered, in the analysis which follows the selection of the optimal input pixel size concerned only the ROIs co-located with the in situ data.

Wind fields at 5 km output resolution were not explored due to: a) lack of NWP model data availability for the Wadden Sea site; b) limited number of in situ measurements for the Camargue area. For the latter site, the comparison between SSW fields and in situ data concerned both EW and IW products. For both the Wadden Sea and Camargue sites, at 12.5 km output resolution, the optimal input pixel size values were 80 m and 160 m for IW and EW images, respectively.

5.2.1. Wind direction

Table 3 presents the RMSE and MBE values obtained for the Wadden Sea area, by comparing LG-Mod and ECMWF wind direction estimates with ground truth data. The statistics obtained, for this area, indicates that both LG-Mod and ECMWF directional estimates are in agreement with the KNMI in situ measurements. However, the RMSE value obtained by the LG-Mod resulted lower than the one from ECMWF: i.e.,

Table 3

Wadden Sea site wind directions from both the ECMWF model and the SAR LG-Mod method at 12.5 km grid, with respect to KNMI in situ observation. $ME^{TH} = 10°$ (and $\alpha = 0.05$).

		ECMWF wind direction	LG-Mod wind direction
Wadden Sea	RMSE [°]	14.0	9.4
	MBE [°]	−2.7	−7.3
Camargue	RMSE [°]	29.3	15.0
	MBE [°]	−23.7	−12.4

9.4° and 14.0°, respectively.

Moreover, the LG-Mod directions were biased with respect to the KNMI ones. The MBE value obtained (−7.3°) can be explained considering that the wind rows used, for wind direction extraction by the LG-Mod, are generally oriented between the direction of the geostrophic and the mean sea surface winds (Alpers and Brümmer, 1994). Instead the ECMWF direction presents no significant bias (−2.7°).

The data presented in Fig. 6a indicates that the selection of the optimal pixel size (i.e., 80 m) through ME_α^{ROI} can reduce the RMSE value up to 7°.

Table 3 presents wind direction summary statistics for the Camargue site. The data shown suggest that for wind direction retrieval the LG-Mod can perform better than the ECMWF: RMSE = 15.0°, MBE = 12.4° and RMSE = 29.3°, MBE = -23.7°, respectively.

It must be observed that the selection of the optimal pixel size (i.e., 80 m and 160 m for IW and EW data, respectively) through ME_α^{ROI} can significantly reduce the RMSE value also for this site (Fig. 6b).

5.2.2. Wind speed

Table 4 presents summary statistics obtained through the comparison of in situ wind speed data with the wind speed values from both the ECMWF model and the inversion of SAR NRCS through CMOD5.N. The LG-Mod (SAR_LG-Mod), the ECMWF model (SAR_ECMWF) and the in situ (SAR_in situ) directions were used as input to the inversion procedure of CMOD5.N.

With regard to the Wadden Sea, it should be noted that:

1. The RMSE value derived from ECMWF wind speeds is quite high, that is 6.0 m/s. This value is almost three times higher than the ones typically reported for open seas, i.e. about 2 m/s (Portabella et al., 2002). The negative MBE value reported in Table 4 (−5.7 m/s) indicates a considerable under-estimation of wind speed by ECMWF. The high value of the MBE found may be due to the dominant role played on the one hand by local orography; on the other by the lack of adequate modelling of the marine boundary layer characterizing coastal areas (Cavaleri and Sclavo, 2006).
2. The combined use of ECMWF wind direction and Sentinel-1 NRCS data, through CMOD5.N, can improve significantly wind speed estimation, with a reduction of both the RMSE (2.4 m/s) and MBE (−0.4 m/s) values (Table 4).
3. The use of the wind direction retrieved by LG-Mod in the CMOD5.N inversion, brought to an additional reduction of the RMSE value (2.2 m/s). The negative MBE value reported (−1.1 m/s) indicates a limited under-estimation of wind speed.
4. The exploitation of the KNMI wind direction, as input to CMOD5.N, gives the lowest values for both RMSE (1.4 m/s) and MBE (−0.1 m/s).

The data reported for the Camargue area (Table 4), show that the lowest RMSE value (1.9 m/s) was obtained by exploiting the wind direction retrieved by LG-Mod in the CMOD5.N inversion. For this site, the RMSE reduction with respect to the use of ECMWF direction is more significant than the one obtained for the Wadden Sea, 42.4% and 8.3% respectively. This difference may be due to the Camargue site orographic complexity which is problematic to be adequately described by
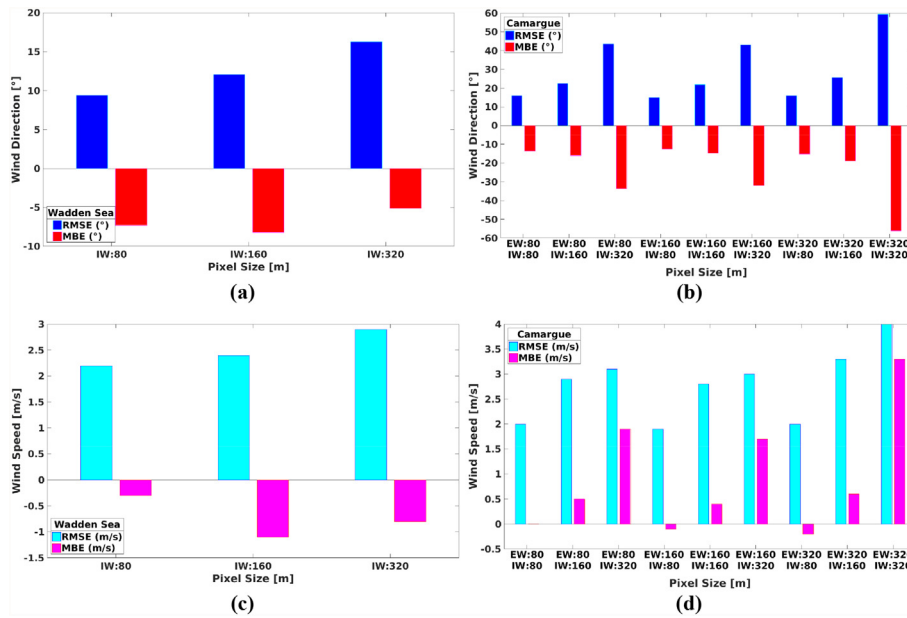
Fig. 6. Statistics obtained at different pixel sizes for both wind direction (a and b) and speed (c and d) for Wadden Sea and Camargue, respectively.

NWP models. It is worth noting that the selection of the optimal pixel size through ME_α^{ROI} can reduce the RMSE value up to 0.7 m/s for the Wadden Sea (Fig. 6c) and to 2.1 m/s for the Camargue (Fig. 6d) site.

5.3. Comparison of SAR SSW fields and NWP model data at different spatial resolutions

Table 5 presents the RMSE and MBE values obtained considering all the ROIs analyzed in the retrieval of SSW fields by means of: 1) the LG-Mod (direction) followed by the CMOD5.N (speed), 2) the NWP model (direction) followed by the CMOD5.N (speed) and 3) the NWP model (direction and speed). The output values of the latter model were assumed as reference.

Directional estimates from the LG-Mod were derived through the reliability threshold adopted in this study, i.e. $ME^{TH} = 10°$.

The results shown in Table 5 indicate a rather close agreement (RMSE $=14.0°$) between the LG-Mod and the ECMWF direction estimates, for the Wadden Sea area. This agreement is supported by the findings from validation statistics in Table 3 where both LG-Mod and ECMWF appeared comparable with KNMI in situ observations. As suggested in Section 5.2, the flat orography and the prevailing winds, blowing along- and on-shore in the dataset analyzed for the Wadden Sea region, may have contributed favorably in the ECMWF directional estimation.

The use of Sentinel-1 NRCS data provide wind speed values which, on average, are significantly higher than those obtained from the ECMWF model (Table 5). Summary statistics show that this behaviour can occur when using either the LG-Mod or the ECMWF wind direction as input to the CMOD5.N inversion.

For the Camargue site, the RMSE of the wind direction estimation by using EW dataset resulted larger than the one obtained from IW,

19.9° and 18.8°, respectively, at 12.5 km. The latter value, is instead larger than the one obtained for the Wadden Sea area, namely 18.8° against 14.0°. In fact, considering the IW dataset, less agreement between LG-Mod and ECMWF direction estimation can be observed for the Camargue respect to the Wadden Sea. The difference reported may be due to the complex orography of the Camargue region as well as to the dominant winds, i.e., the Tramontane and the Mistra, which blow from land to sea.

At high resolution (5 km grid) wind direction RMSE value (15.0°) for IW images shows a fairly close agreement between LG-Mod and SKIRON (Table 5). On the contrary, a higher RMSE value (23.2°) can be observed for EW images. This result may depend on the lower native resolution of EW images (i.e., 40 m × 40 m) compared to the IW ones (i.e., 10 m × 10 m).

The higher native spatial resolution of IW images appears to provide more directional information than the EW products. This consideration is confirmed also by ROI selection percentages (84.5% against 30.1%, respectively).

The exploitation of S-1 NRCS for CMOD5.N inversion provides wind speed estimates that compare better with the values obtained through SKIRON than with those obtained from ECMWF, independently of the input direction adopted. For both EW and IW data, the wind speed values obtained by SAR result over-estimated in comparison to those provided by both NWP models.

5.3.1. Spectral analysis

A spectral analysis of SAR and NWP model winds at high and medium resolution was carried out to evaluate both the impact of output spatial resolution and SAR on the spectral properties of the winds retrieved (Karagali et al., 2013; Vogelzand et al., 2011).

Fig. 7 shows the average power spectra as a function of

Table 4

Comparison of wind speeds obtained at 12.5 km grid from ECMWF and those from the inversion of SAR NRCS exploiting each wind direction, namely, from KNMI (SAR$_{in\ situ}$), ECMWF (SAR$_{ECMWF}$) and SAR LG-Mod (SAR$_{LG-Mod}$), as input to CMOD5.N, against KNMI in situ observations. Wadden Sea Site.

		ECMWF wind speed	SAR$_{in\ situ}$ wind speed	SAR$_{ECMWF}$ wind speed	SAR$_{LG-Mod}$ wind speed
Wadden Sea	RMSE [m/s]	6.0	1.4	2.4	2.2
	MBE [m/s]	−5.7	−0.1	−0.4	−1.1
Camargue	RMSE [m/s]	3.5	2.2	3.3	1.9
	MBE [m/s]	−1.6	−1.9	1.3	−0.1

Table 5
Comparison at 12.5 km grid of: (i) wind directions obtained from SAR LG-Mod with $ME^{TH} = 10°$ (and $\alpha = 0.05$) and from ECMWF; (ii) the corresponding CMOD5.N-derived wind speeds and the one from ECMWF.

	Sites	S-1 products	LG-Mod wind direction		SAR_{LG-Mod} wind speed		SAR_{NWP} wind speed		Sample number N ($ME^{TH} = 10°$)
			RMSE [°]	MBE [°]	RMSE [m/s]	MBE [m/s]	RMSE [m/s]	MBE [m/s]	
ECMWF	Wadden Sea	IW	14.0	−3.8	5.6	4.7	6.0	5.0	933 ($N^{TOT} = 944$, $P = 98.8\%$)
Max delay ~ −35 min									
Spatial grid ~12.5 km	Camargue	EW	19.9	−11.0	7.7	5.7	6.4	4.0	1299 ($N^{TOT} = 1505$, $P = 86.3\%$)
		IW	18.8	6.6	6.0	4.6	8.3	6.2	551 ($N^{TOT} = 552$, $P = 99.8\%$)
SKIRON	Camargue	EW	23.2	−8.2	6.4	3.7	6.0	2.7	2949 ($N^{TOT} = 9797$, $P = 30.1\%$)
Max delay ~ −16 min									
Spatial grid ~5 km		IW	15.0	−5.1	3.6	2.8	3.7	2.0	3308 ($N^{TOT} = 3792$, $P = 87.2\%$)

wavenumber (bottom axis) and wavelength (top axis) in a log-log scale, along the zonal u (a and c) and meridional v (b and d) components of winds. The plots refer to SAR winds, with LG-Mod (SAR_{LG-Mod}) and NWP model directions (SAR_{ECMWF} and SAR_{SKIRON}), as well as NWP models winds, for both sites.

With respect to the Camargue site, Fig. 7a and b indicate that, at a fixed spatial resolution of either 5 km or 12.5 km SAR_{LG-Mod} wind spectra show a higher spectral density than SAR_{ECMWF} and SAR_{SKIRON} winds, respectively. In its turn, the relative spectra present a higher spectral density than that obtained for ECMWF and SKIRON winds, respectively.

SAR_{LG-Mod} winds, wind fields obtained by inverting the SAR NRCS using NWP models directions (SAR_{ECMWF} and SAR_{SKIRON}) and wind fields from NWP models show a spectral density higher, for high resolution outputs (5 km), with respect to that obtained at medium resolution (12.5 km). These considerations apply to both u and v wind components.

Even though SKIRON data are unavailable for the Wadden Sea, the above mentioned comments may be considered valid also for this site (Fig. 7c and d).
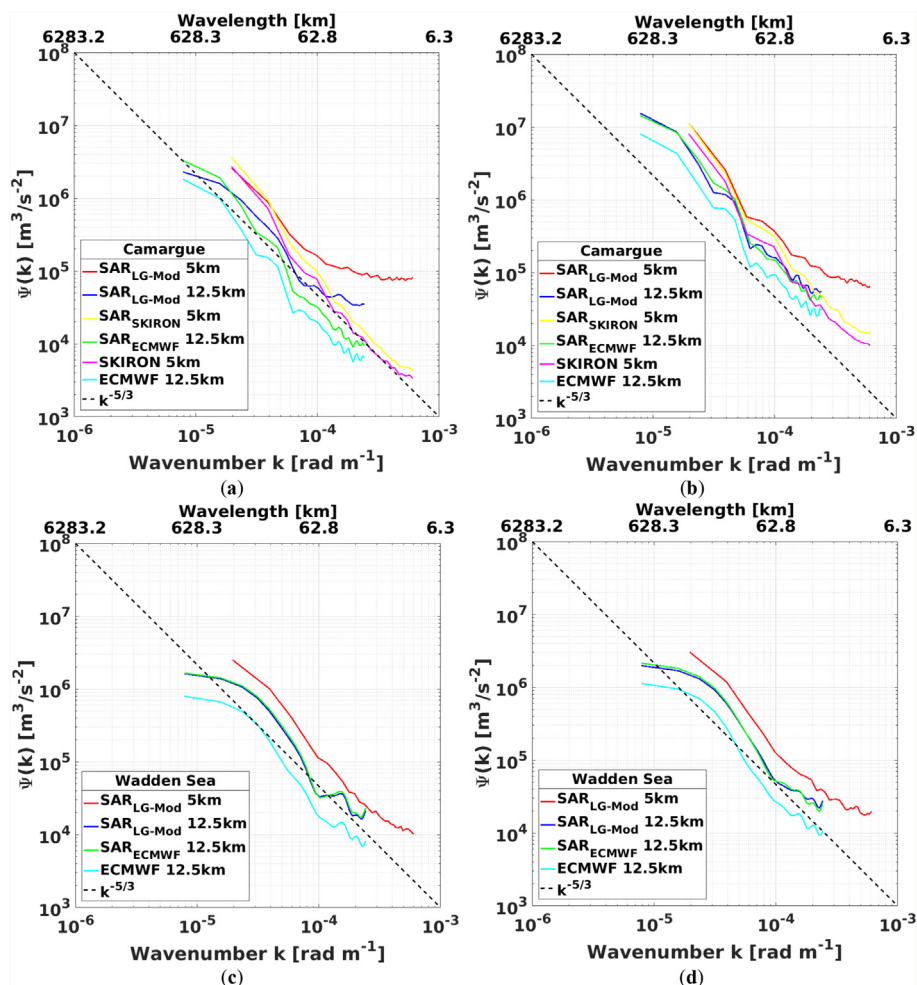

Fig. 7. Averaged power spectra Ψ as a function of wavenumber k (lower axis) and wavelength (upper axis), in a log-log scale along the (a) zonal (west – east) and the (b) meridional (south – north) directions for Camargue site. The same spectra are plotted for the Wadden Sea site (c and d). The black lines indicate the −5/3 slopes.

Table 6

Spectral slopes for SAR and NWP models wind fields. The variation from the −5/3 law is defined as 100 × (−5/3-slope)/(−5/3).

	Slope		Variation from −5/3 (%)	
	U-component	V-component	U-component	V-component
Camargue				
SAR$_{LG\text{-}Mod}$ 5 km	−0.82	−1.29	50.8	22.6
SAR$_{LG\text{-}Mod}$ 12.5 km	−1.38	−1.77	17.2	−6.2
SAR$_{SKIRON}$ 5 km	−1.93	−1.86	−15.8	−11.6
SAR$_{ECMWF}$ 12.5 km	−1.88	−1.88	−12.8	−12.8
SKIRON 5 km	−1.90	−1.86	−14.0	−11.6
ECMWF 12.5 km	−1.79	−1.78	−7.4	−6.8
Wadden Sea				
SAR$_{LG\text{-}Mod}$ 5 km	−1.62	−1.46	2.8	12.4
SAR$_{LG\text{-}Mod}$ 12.5 km	−1.64	−1.60	1.6	4.0
SAR$_{ECMWF}$ 12.5 km	−1.63	−1.66	2.2	0.4
ECMWF 12.5 km	−1.65	−1.67	1.0	−0.2

Table 6 shows spectral slopes estimated for each wind product. As can be observed, slope values range from −0.82 to −1.93.

For the Camargue site, $SAR_{LG\text{-}Mod}$ slopes are flatter for very high resolution and become steeper as the resolution decreases. At a fixed spatial resolution $SAR_{LG\text{-}Mod}$ slopes are flatter than those obtained either by NWP models or by using NWP model directions in conjugation with SAR NRCS. Flatter slopes indicate a smaller energy deficit for increasing wavenumbers. Thus, smaller length scales can be resolved by the SAR product. This finding demonstrates the higher effective spatial resolution achievable by the SAR retrieved winds with respect to those resulting when using NWP models. The smallest deviation from −5/3 law is obtained for the u component by ECMWF and for the v component by $SAR_{LG\text{-}Mod}$. The discrepancies from the −5/3 law increase with increasing spatial resolution.

6. Discussion

6.1. Wind direction accuracy map

Each wind direction map obtained in our study is associated with an ME^{ROI} map representing the wind direction accuracy for each ROI in the map. The accuracy map thus obtained may be considered an added-value product respect to the quality measurements provided by Copernicus (Mouche, 2011). As well known, the wind field maps available through Copernicus rely on statistical Bayesian inversion whose a-priori information is derived from NWP models (Mouche, 2011). The resulting maps are provided with a wind quality flag based on the combination of two terms. The first depends on the percentage of bright targets detected in the SAR image within the cell; the second relates to the consistency between ancillary NWP model output and the NRCS used in the wind inversion scheme (Mouche, 2011). As a result, the lower the minimum value of the cost function defined in the Bayesian procedure, the better is such consistency and the higher must be the confident level of the inverted wind vector (Mouche, 2011).

It seems worth recalling that in complex coastal areas, NWP models may fail to retrieve SSW adequately (Zecchetto and Accadia, 2014). This can affect the quality flag provided by Copernicus. Since the definition of wind direction accuracy map provided by LG-Mod is only related to the directional content of the SAR cell considered, this approach can prove useful to describe all possible local wind conditions independently of NWP models.

6.2. Input pixel size selection

To our knowledge, only Du et al. (2002) have used the Discrete Wavelet Transforms (DWT) to calculate at different scales a directional factor which could define the optimal scale. Leite et al. (2010) and Zecchetto and De Biasio (2008) have proposed approaches whereby the modulation frequencies not belonging to either BLR or WS ranges are attenuated. However, no selection of the optimal scale has been suggested. In the original LG method (Koch, 2004) the optimal pixel-size selection was carried out a posteriori by considering the pixels size providing the direction closest to in situ data (Koch and Feser, 2006).

The LG-Mod results reported in our study (Section 5.2) indicate that the pixel size selection criterion which is based on the use of ME_α^{ROI} can improve the retrieval of both wind direction and speed (Fig. 6). Even though our approach is a first attempt and in need of further investigation, the results reported encourage the suggestion that ME_α^{ROI} may be fruitfully used for the development of a multi-scale procedure based on local gradient.

6.3. Sentinel −1 IW and EW comparison

The results obtained from the directional analysis (Section 5.1) suggest that Sentinel-1 IW images may be suitable for high resolution SSW retrieval, in complex coastal areas. Actually, the findings reported indicate that IW images can guarantee good LG-Mod performance in terms of overall directional accuracy percentage of reliable estimates at both high and medium resolution, 84.5% and 99.2%, respectively. In case of high output resolution, the use of EW images can yield less satisfying directional results, than the ones obtained for medium resolution, i.e. 30.1% and 86.3% of reliable estimates, respectively.

The results of the Directional Analysis to estimate the effectiveness of both EW and IW in SSW retrieval are confirmed by the comparison of SAR SSW fields with in situ data (Section 5.2). Undoubtedly, the better results obtained for the Wadden Sea site using only IW, compared to the findings for the Camargue site employing IW and EW data, may depend on both the different orography and the local prevailing wind conditions characterizing the two regions. An additional reason for the difference observed may issue from the use of EW data only for the Camargue site. The higher resolution of IW images appears to yield more directional information than the one obtained through EW images, with a consequent better performance for the LG-Mod estimation (Table 3). This finding seems to confirm the claim by La et al. (2017) stating that, at high spatial resolution (up to 5 km), accurate wind fields are difficult to be obtained from S-1 EW images. In addition, La et al. (2017) also suggest that EW data should be exploited for the extraction of wind fields at higher resolutions.

6.4. SSW fields validation through in situ data

The LG-Mod wind direction estimates reported in Table 3 are in agreement with those obtained by La et al. (2017) even though their data refer to wind directions retrieved in coastal areas from S-1 using the original LG method. Carvajal et al. (2014) used a modified LG algorithm to analyze ENVISAT ASAR data. In their study, these authors report a significantly higher RMSE value compared to ours (Table 3). The difference between the data reported by Carvajal et al. (2014) and those obtained by both La et al. (2017) and us may depend on the use of different SAR data. Actually, the Performance Indicator of S-1 is higher than the one reported for ENVISAT ASAR data (ESA, 2012).

When using in situ direction to retrieve SAR wind speed, our results confirm the ones obtained by Takeyama et al. (2013) through the same procedure with ENVISAT ASAR data in two different coastal areas.

For both sites investigated in our study, when using the LG-Mod direction for wind speed retrieval, the results indicate a lower performance (Table 4) with respect to that reported by La et al. (2017) (RMSE = 1.59 m/s). This finding may be due to the fact that La et al.

(2017) considered only low-average wind regimes (up to 15 m/s), whereas our image dataset also includes average-high wind regimes (above 15 m/s). In high wind regimes wind direction retrieval errors are expected to have marked impact in wind speed estimation (La et al., 2017).

When we used the NWP model wind direction as input to CMOD5.N, wind speed retrieval performances may have been influenced by both the specific site orography and the prevailing local winds. The statistics presented in Table 4 seem to support the reliability of ECMWF wind direction for SAR wind speed retrieval in the flat Wadden Sea area generally characterized by along- and on-shore dominant winds. When the wind blows from land to sea and in cases of marked orography, such as the one of the Camargue site, wind direction estimates from NWP models may not be reliable for SAR CMOD5.N inversion (Adamo et al., 2014).

6.5. Wind spatial variability

As well knowns, the analysis of the spectral density as a function of wavenumber can give relevant information about the energetic contribution of processes which occur at corresponding length scales. Moreover, the spectral density decay slope can provide details on the sensitivity of the different wind products to the scale of wind features. Hence, the results of the slope analysis can lead to the identification of the output spatial resolution able to represent wind variability.

The results presented in our study, indicate that SAR winds, retrieved at both 5 km and 12.5 km resolution, can be suitable for the description of small scale phenomena. Indeed, SAR_{LG-Mod} spectral slopes obtained are flatter compared not only to the ones from NWP models, but also to those obtained when the directions from NWP models are used, in the SAR NRCS inversion, for wind speed retrieval (SAR_{ECMWF} and SAR_{SKIRON}) (Table 6). According to Karagali et al. (2013), this finding can be explained by considering that smaller scales are better represented in SAR products. In our study, the flattest slope was achieved when using the LG-Mod direction.

A general decrease of spectral density at decreasing spatial resolution of SAR wind fields is evidenced in Fig. 7. This finding is in agreement with Karagali et al. (2013).

In our study, the spectral density obtained for SKIRON is higher than the one from ECMWF. This result may be due, on the one hand to the better spatial resolution of the SKIRON with respect to ECMWF, and on the other hand to the fact that SKIRON is a model optimised for the Mediterranean Sea. Actually, if specific processes such as those related to the boundary layer are not included in a model, the wind spatial variability will not be adequately represented independently from the spatial resolution of the model used (Anonymous Reviewer).

Drawing on global spectral data (Nastrom and Gage, 1985), Lindborg (1999) proposed the $-5/3$ theoretical law to describe the spectral density decay. This law can be applied at the meso-scale (Larsén et al., 2013). Kargali et al. (2013) warn that the area extension may influence spectral analysis results. Thus, the discrepancies between our data and those expected according to $-5/3$ law (Table 6) may depend on the fact that our analysis covers a restricted area.

Moreover, since the areas investigated in the present study are costal areas characterized by variable wind fields, the spectral analysis results will consequently differ from the ones expected for meso-scale. This consideration is supported by the finding that the discrepancies found for the Wadden Sea area are smaller than those obtained for the Camargue site (Table 6).

7. Conclusions

The findings reported in our study prove the usefulness of Sentinel-1 products for the retrieval of SSW direction and wind speed in coastal areas even if these are characterized by different orographic and meteorological conditions. The results reported were evaluated and compared with both in situ measurements and NWP models. They prove the effectiveness of the LG-Mod ME_α^{ROI} parameter for providing: a) a quality map of the retrieved wind direction outputs; b) the selection of the optimal pixel size; c) a threshold value, i.e. ME^{TH}, to identify reliable wind direction estimates. Both wind and speed accuracy maps are required by end users for the assimilation of satellite products not only for modelling purposes but also for decision making. A forthcoming study will focus on whether wind speed accuracy maps can be analytically obtained from the exploitation of ME_α^{ROI} maps.

The LG-Mod algorithm can provide reliable and high resolution S-1 SSW fields in spite of the constrains arising from poor wind rows visibility on SAR imagery. Hence, the use of S-1 data and LG-Mod could enhance and complement NWP models for the implementation of an operational system useful in the monitoring of coastal areas winds. SAR data could be exploited for three purposes: 1) to drive the downscale of NWP model winds up to few km resolutions; 2) to correct the systematic biases characterizing NWP model estimation; 3) to increase the frequency of wind observations along with the estimation obtained by NWP models, especially during extreme storm events. The spectral analysis findings suggest that SAR winds may improve NWP models through data assimilation.

Although based on a limited number of Sentinel-1 images and in situ measurements, the results presented in this study may be considered an additional contribution in the evaluation of coastal wind direction and speed derived either from SAR or NWP models.

Undoubtedly, the development of an adequate and dense European network of coastal wind measurement stations would be of great help for SAR SSW fields validation. It is hoped that the in situ component of the Copernicus project will provide support for validation purposes.

Appendix A. Supplementary data

Supplementary data to this article can be found online at https://doi.org/10.1016/j.rse.2019.03.019.

References

Adamo, M., Rana, F.M., De Carolis, G., Pasquariello, G., 2014. Assessing the Bayesian inversion technique of C-band synthetic aperture radar data for the retrieval of wind fields in marine coastal areas. J. Appl. Rem. Sens. 8 (1), 083531.

Ahsbahs, T.T., Badger, M., Karagali, I., Larsén, X.G., 2017. Validation of sentinel-1A SAR coastal wind speeds against scanning LiDAR. Remote Sens. 9 (6). https://doi.org/10.3390/rs9060552.

Alpers, W., Brümmer, B., 1994. Atmospheric boundary layer rolls observed by the synthetic aperture radar aboard the ERS-1 satellite. J. Geophys. Res. 99 (C6), 12613–12621.

Benassai, G., Migliaccio, M., Nunziata, F., 2015. The use of COSMO-SkyMed© SAR data for coastal management. J. Mar. Sci. Technol. 20, 542–550.

Borrelli, P., Lugato, E., Montanarella, L., Panagos, P., 2017. A new assessment of soil loss due to wind erosion in European agricultural soils using a quantitative spatially distributed modelling approach. Land Degrad. Develop. 28, 335–344.

Carvajal, G.K., Eriksson, L.E.B., Ulander, L.M.H., 2014. Retrieval and quality assessment of wind velocity vectors on the ocean with C-band SAR. IEEE Trans. Geosci. Remote

Sens. 52 (5), 2519–2537.

Cavaleri, L., Sclavo, M., 2006. The calibration of wind and wave model data in the Mediterranean Sea. Coast. Eng. 53 (7), 613–627.

CPSL, 2005. Coastal protection and sea level rise - solutions for sustainable coastal protection in the Wadden Sea region. Wadden Sea ecosystem no. 21. In: Common Wadden Sea Secretariat, Trilateral Working Group on Coastal Protection and Sea Level Rise (CPSL), Wilhelmshaven,Germany, . http://www.waddensea-secretariat.org/sites/default/files/downloads/cpsl-ii-2005.pdf.

Dagestad, K. F., Horstmann, J., Mouche, A., Perrie, W., Shen, H., Zhang, B., … and Badger, M. (2012, June). Wind retrieval from synthetic aperture radar — an overview. In Proceedings of the 4th SAR Oceanography Workshop (SEASAR 2012), Tromsø, Norway (pp. 18–22).

Dankert, H., Horstmann, J., Rosenthal, W., 2003. Ocean wind fields retrieved from radar-image sequences. J. Geophys. Res. Oceans (C11), 108.

Dee, D.P., Uppala, S.M., Simmons, A.J., Berrisford, P., Poli, P., Kobayashi, S., Bechtold, P., 2011. The ERA-interim reanalysis: configuration and performance of the data assimilation system. Q. J. R. Meteorol. Soc. 137 (656), 553–597.

Drobinski, P., Foster, R.C., 2003. On the origin of near-surface streaks in the neutrally-stratified planetary boundary layer. Bound.-Layer Meteorol. 108 (2), 247–256.

Du, Y., Vachon, P.W., Wolfe, J., 2002. Wind direction estimation from SAR images of the ocean using wavelet analysis. Can. J. Remote. Sens. 28 (3), 498–509.

ESA SP-1322/1, 2012. In: Fletcher, K. (Ed.), Sentinel-1: ESA's Radar Observatory Mission for GMES Operational Services. 978-92-9221-418-0, .

Fichaux, N., Ranchin, T., 2002. Combined extraction of high spatial resolution wind speed and wind direction from SAR images: a new approach using wavelet transform. Can. J. Remote. Sens. 28 (3), 510–516.

Fisher, N.I., 1993. Statistical Analysis of Circular Data. Cambridge UP, Cambridge, UK.

Hersbach, H., 2010. Comparison of C-band scatterometer CMOD5.N equivalent neutral winds with ECMWF. J. Atmos. Ocean. Technol. 27 (4), 721–736.

Horstmann, J., Koch, W., 2004. Evaluation of an operational SAR wind field retrieval algorithm for ENVISAT ASAR. In: Geoscience and Remote Sensing Symposium, 2004. IGARSS'04. Proceedings. 2004 IEEE International, vol. 1 IEEE.

Kallos, G., Nickovic, S., Papadopoulos, A., Jovic, D., Kakaliagou, O., Misirlis, N., … Anadranistakis, E., 1997. The regional weather forecasting system SKIRON: an overview. In: Proceedings of the Symposium on Regional Weather Prediction on Parallel Computer Environments. vol. 15. pp. 17.

Karagali, et al., 2013. Spectral Properties of ENVISAT ASAR and QuikSCAT Surface Winds in the North Sea. Remote Sensing 5 (11), 6096–6115.

Koch, W., 2004. Directional analysis of SAR images aiming at wind direction. IEEE Trans. Geosci. Remote Sens. 42 (4), 702–710.

Koch, W., Feser, F., 2006. Relationship between SAR-derived wind vectors and wind at 10-m height represented by a mesoscale model. Mon. Weather Rev. 134 (5), 1505–1517.

Komarov, A.S., Zabeline, V., Barber, D.G., 2014. Ocean surface wind speed retrieval from C-band SAR images without input of wind direction. IEEE Trans. Geosci. Remote Sens. 52 (2), 980–990.

La, T.V., Khenchaf, A., Comblet, F., Nahum, C., 2017. Exploitation of C-band Sentinel-1 images for high-resolution wind field retrieval in coastal zones (Iroise coast, France). J. Sel. Top. Appl. Earth Obs. Remote Sens 10 (12).

Larsén, X.G., Vincent, C., Larsen, S., 2013. Spectral structure of mesoscale winds over the water. Q. J. R. Meteorol. Soc. 139 (672), 685–700.

Leite, G.C., Ushizima, D.M., Medeiros, F.N., De Lima, G.G., 2010. Wavelet analysis for wind fields estimation. Sensors 10 (6), 5994–6016.

Levy, G., 2001. Boundary layer roll statistics from SAR. Geophys. Res. Lett. 28 (10), 1993–1995.

Li, X.M., Lehner, S., 2014. Algorithm for sea surface wind retrieval from TerraSAR-X and TanDEM-X data. IEEE Trans. Geosci. Remote Sens. 52 (5), 2928–2939.

Lindborg, E., 1999. Can the atmospheric kinetic energy spectrum be explained by two-dimensional turbulence? J. Fluid Mech. 388, 259–288.

Liu, T., Tang, W., 1996. Equivalent neutral wind. Jet Propulsion Laboratory Publ. (96-17), 1–22.

Liu, W.T., Katsaros, K.B., Businger, J.A., 1979. Bulk parameterization of air-sea exchanges of heat and water vapor including the molecular constraints at the interface. J. Atmos. Sci. 36 (9), 1722–1735.

Liu, G., Yang, X., Li, X., Zhang, B., Pichel, W., Li, Z., Zhou, X., 2013. A systematic comparison of the effect of polarization ratio models on sea surface wind retrieval from C-band synthetic aperture radar. IEEE J. Sel. Top. Appl. Earth Obs. Remote Sens. 6 (3), 1100–1108.

Millot, C., 1979. Wind induced upwellings in the Gulf of Lions. Oceanol. Acta 2 (3), 261–274.

Monaldo, F.M., Jackson, C.R., Pichel, W.G., 2013. Seasat to Radarsat-2: research to operations. Oceanography 26 (2), 34–45.

Monaldo, F., Jackson, C., Pichel, W., Li, X., 2015. Early validation of operational SAR wind retrievals from Sentinel-1A. In: 2015 IEEE International Geoscience and Remote Sensing Symposium (IGARSS). IEEE, pp. 1223–1226.

Mouche, A., 2010. Sentinel-1 ocean wind fields (OWI) algorithm definition. In: Sentinel-1 IPF Reference: (S1-TN-CLS-52-9049) Report; CLS-DAR-NT-10-167.

Mouche, A., Collard, F., Chapron, B., Dagestad, K.-F., Guitton, G., Johannessen, J.A., Kerbaol, V., Hansen, M.W., 2012. On the use of Doppler shift for sea surface wind retrieval from SAR. IEEE Trans. Geosci. Remote Sens. 50 (7), 2901–2909.

Nastrom, G.D., Gage, K.S., 1985. A climatology of atmospheric wavenumber spectra of wind and temperature observed by commercial aircraft. J. Atmos. Sci. 42 (9), 950–960.

Nederlands, K., 2000. Handbook for the Meteorological Observation.

Pichel, W.G., Monaldo, F.M., Jackson, C., Li, X., Sapper, J., 2015. NOAA operational SAR winds – Current status and plans for sentinel-1A. In: 2015 IEEE International Geoscience and Remote Sensing Symposium (IGARSS). IEEE, pp. 4916–4919.

Portabella, M., Stoffelen, A., 2009. On scatterometer ocean stress. J. Atmos. Ocean. Technol. 26 (2), 368–382.

Portabella, M., Stoffelen, A., Johannessen, J.A., 2002. Toward an optimal inversion method for sythentic aperture radar wind retrieval. J. Geophys. Res. 107 (C8), 3086. https://doi.org/10.1029/2001JC000925.

Rana, F.M., Adamo, M., Pasquariello, G., De Carolis, G., Morelli, S., 2016. LG-Mod: a modified Local Gradient (LG) method to retrieve SAR Sea surface wind directions in marine coastal areas. J. Sens. 2016, 9565208. https://doi.org/10.1155/2016/9565208. (7 pages).

Stoffelen, A., Anderson, D., 1997. Scatterometer data interpretation: estimation and validation of the transfer function CMOD4. J. Geophys. Res. Oceans 102 (C3), 5767–5780.

Svensson, N., Sahlée, E., Bergström, H., Nilsson, E., Badger, M., Rutgersson, A., 2017. A case study of offshore advection of boundary layer rolls over a stably stratified sea surface. Adv. Meteorol. 2017, 9015891. https://doi.org/10.1155/2017/9015891.

Takeyama, Y., Ohsawa, T., Kozai, K., Hasager, C.B., Badger, M., 2013. Comparison of geophysical model functions for SAR wind speed retrieval in Japanese coastal waters. Remote Sens. 5, 1956–1973. https://doi.org/10.3390/rs5041956.

Thompson, D.R., Elfouhaily, T.M., Chapron, B., 1998. Polarization ratio for microwave backscattering from the ocean surface at low to moderate incidence angles. In: Geoscience and Remote Sensing Symposium Proceedings, 1998. IGARSS'98. 1998 IEEE International, vol. 3. IEEE, pp. 1671–1673.

Vachon, P.W., Dobson, F.W., 2000. Wind retrieval from RADARSAT SAR images: selection of a suitable C-band HH polarization wind retrieval model. Can. J. Remote. Sens. 26 (4), 306–313.

Vogelzang, J., Stoffelen, A., Verhoef, A., 2011. On the quality of high-resolution scatterometer winds. J. Geophys. Res. Oceans 116 (C10).

Wackerman, C.C., Pichel, W.G., Clemente-Colon, P., 2003. Automated estimation of wind vectors from SAR. In: Proceedings of the 12th Conference on Interactions of the Sea and Atmosphere.

Zecchetto, S., Accadia, C., 2014. Diagnostics of T1279 ECMWF analysis winds in the Mediterranean Basin by comparison with ASCAT 12.5 km winds. Q. J. R. Meteorol. Soc. 140 (685), 2506–2514.

Zecchetto, S., De Biasio, F., 2008. A wavelet-based technique for sea wind extraction from SAR images. Geoscience and Remote Sensing, IEEE Transactions on 46 (10), 2983–2989.

Zecchetto, S., De Biasio, F., Della Valle, A., Cucco, A., Quattrocchi, G., Cadau, E., 2016. Wind fields from COSMO-SKYMED and Radarsat-2 SAR in coastal areas. In: 2015 IEEE International Geoscience and Remote Sensing Symposium (IGARSS). IEEE, pp. 1535–1538.

Zhang, B., Perrie, W., Vachon, P.W., Li, X., Pichel, W.G., Guo, J., He, Y., 2012. Ocean vector retrieval from C-band fully polarimetric SAR measurements. IEEE Trans. Geosci. Remote Sens. 50 (11), 4252–4261.

Zhao, Y., Li, X.M., Sha, J., 2016. Sea surface wind streaks in spaceborne synthetic aperture radar imagery. J. Geophys. Res. Oceans 121 (9), 6731–6741.

Zodiatis, G., Lardner, R., Georgiou, G., Demirov, E., Manzella, G., Pinardi, N., 2003. An operational European global ocean observing system for the eastern Mediterranean Levantine basin: the Cyprus coastal ocean forecasting and observing system. Mar. Technol. Soc. J. 37 (3), 115–123.